Dalton Transactions

ROYAL SOCIETY OF CHEMISTRY

PAPER

View Article Online
View Journal | View Issue

Cite this: *Dalton Trans.*, 2026, **55**, 3866

Stability *vs.* activity in electrocatalytic hydrogen production and magnetic studies of mononuclear labile Cu(II) and Ni(II) complexes†

Maria A. Bhatti, [a] Luca M. Carrella, [a] Carsten Streb, [a] Eva Rentschler *[a] and Sriram Sundaresan *[a,b]

Received 22nd January 2026,
Accepted 4th February 2026

DOI: 10.1039/d6dt00175k

rsc.li/dalton

In this study, two new mononuclear Schiff base salen-derived complexes, $[Cu^{II}(H_2L^{Me})]\cdot 1.5H_2O$ (**C1**) and $[Ni^{II}(H_2L^{Me})]\cdot 3H_2O$ (**C2**), were prepared from 2,6-bis(hydroxymethyl)-4-methylphenol H_4L and characterised by single crystal X-ray diffractometry, infrared spectroscopy and elemental analysis. Electrochemical studies in DMF with acetic acid as a proton source revealed catalytic hydrogen evolution activity for both complexes, with **C1** displaying higher activity, lower overpotential (η = 0.71 V), and a higher TOF_{max} of 452 029 s^{-1} compared to **C2** (η = 0.89 V, TOF_{max} = 986 s^{-1}). The stability of the compounds was tested *via* controlled potential electrolysis (CPE) and rinse tests, indicating partial heterogeneous contributions to catalysis from electrode-deposited species. These deposits were further analysed by SEM and EDX. To rule out the possibility of nanoparticle formation, dynamic light scattering DLS analysis was performed.

Introduction

Climate change is one of the most significant threats to the planet. As the global demand for energy increases year by year, the urgent need to transition to sustainable energy sources becomes more and more apparent. Among several renewable alternatives, hydrogen, as a clean and versatile energy carrier, holds an immense potential in decarbonizing various sectors, including transportation and industry.[1–4] However, the widespread adoption of hydrogen as a fuel hinges on overcoming challenges associated with its production, particularly the reliance on costly and scarce catalyst materials. Platinum group metals are so far the best-performing materials to catalyse the hydrogen evolution reaction, however they are not earth abundant and are expensive, which limits their large-scale implementation for a sustainable future.[5,6]

Over the past two decades scientists have been intensively looking for earth abundant and cost-effective catalyst alternatives to replace the noble metal ions for this process. Some of the recent reviews in the literature have nicely summarized the homogeneous catalysts studied.[7–9] Among other first row transition metals, cobalt has emerged as a particularly promising candidate and has been extensively investigated both photocatalytically and electrocatalytically, including mechanistic studies for hydrogen production, due to the availability of various oxidation states such as +1, +2 and +3.[7,9–11] However, the cobalt supply chain presents significant environmental and sustainability challenges and is classified as crucial mineral by EU and USA. Moreover, the mining process of cobalt also has ethical procurement challenges, including poor working conditions and the involvement of child labour. These issues have prompted the search for more sustainable and ethically secure alternatives for a catalyst design. Catalysts based on other 3d metals, including copper and nickel, are comparatively less reported, but their raw materials can be sourced from more sustainable and stable supply chain.[8,12–15] The catalytic process can be performed both in homogeneous as well as heterogeneous ways.[16,17] One of the several advantages of the homogeneous systems is their tunability and possibility of structure function correlation studies.[18–20] On the other hand, homogeneous systems, especially with 3d metal ions suffer from stability issues due to the labile nature of the 3d metals and their rich redox properties.[12,21]

Literature demonstrates that the catalytic performance of 3d metal complexes, like copper and nickel, for the hydrogen evolution reaction (HER) can vary depending on ligand environment and geometry. While copper and nickel complexes offer promise as sustainable alternatives to platinum-group metals in electrocatalytic hydrogen evolution, they often exhibit lower activity, stability and selectivity compared to their noble metal counterparts, necessitating innovative ligand designs and strategies to enhance performance.[22]

[a]*Department Chemie, Johannes-Gutenberg-Universität Mainz, Duesbergweg 10-14, 55128 Mainz, Germany. E-mail: rentschl@uni-mainz.de, sundaresan@fzu.cz*
[b]*Institute of Physics of the , Czech Academy of Sciences, Cukrovarnická 10, 162 00 Prague, Czech Republic*

† Dedicated to Prof. Sally Brooker (University of Otago) on her birthday.

Furthermore, the open-shell nature and flexible oxidation states of these metals can lead to undesired side reactions or catalyst deactivation, complicating mechanistic understanding and control.[23] The catalyst design must be trivial to keep the life cycle assessment (LCA) impact scores of the materials used in the synthesis and testing to a minimum, as well as ensuring the rightful use of biproducts generated. It is a multi-fold challenge to design a sustainable, cost-effective and stable catalyst with enhanced activity using 3d metals, on par with platinum group analogues.

Schiff base ligands based on salen derivatives have attracted significant interest in catalyst design over the past decade due to their ease of synthesis and ability to readily coordinate with a range of 3d metals and have been investigated for various catalytic applications involving different 3d metals.[24,25] Complexes based on cobalt, nickel and copper with salen ligand derivatives are studied for both photo and electrocatalytic HER reactions.[7,26,27]

In this work we report two new potential catalysts (**C1**-Cu(II) and **C2**-Ni(II)) for HER based on a new Schiff base Salen ligand derivate. The ligand design was planned to have free abstractable protons close to the metal centre to aid the catalytic activity. However, during the complexation with the metal, the hydroxy group were methylated from the solvent molecule.

Results and discussion

Synthesis and initial characterization

The ligand H_4**L** was synthesised in two steps from commercially available starting materials. First, 2,6-bis(hydroxymethyl)-4-methylphenol was oxidised in the presence of MnO_2 in chloroform, yielding both monoaldehyde and dialdehyde products (Fig. 1). These were then separated by column chromatography. Subsequently, Schiff base condensation of two equivalents of the monoaldehyde with ethylenediamine was carried out (for detailed procedure, see the Experimental section). The ligand was obtained in high yield as yellow solid and was characterised using a range of techniques including ^{1}H-NMR, ^{13}C-NMR, 2D-NMR, Infrared spectroscopy, mass spectrometry and elemental analysis. In the IR spectroscopy

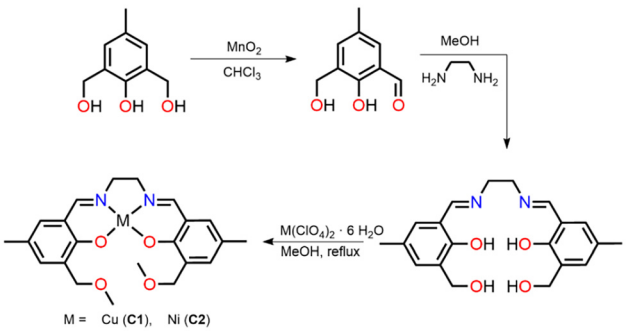

Fig. 1 Two-step synthesis scheme of ligand H_4**L** and complexes **C1** and **C2**.

the presence of prominent a C=N peak around 1628 cm^{-1} corresponding to imine formation and the absence of a signal around 1690 cm^{-1} from the aldehyde clearly indicate the successful formation of the desired Schiff base ligand. Additional key peaks include O–H stretching around 3300 cm^{-1} and C–H stretching vibrations around 2900 cm^{-1} as seen in Fig. S6. In the ^{1}H-NMR spectrum the presence of an imine signal at 8.35 ppm confirms the successful formation of the imine (fully assigned spectra S3). The principal peak at 379.16 and a secondary peak at 357.18 in the ESI mass spectra which corresponds to $[H_4\mathbf{L} + Na]^+$ and $[H_4\mathbf{L} + H]^+$ further confirms the formation of the desired ligand.

The synthesised H_4**L** ligand was reacted with one equivalent of hexahydrate perchlorate metal salt (copper (**C1**); nickel (**C2**)) and was heated in methanol for two hours under reflux. The complex solutions were cooled down to room temperature and were filtered before setting them for slow evaporation. The complexes in both the cases were obtained as needles after one to two weeks. Both complexes were characterised by single crystal X-ray, infrared spectroscopy (Fig. S7 and S8), mass spectrometry (Fig. S12–S15) and elemental analysis. The characterisation data revealed an *in situ* reaction has taken place between the primary hydroxy group of the ligand and the solvent molecule, leading to a rearrangement in the ligand backbone and the formation of a new ether group as shown in Fig. 1.

Crystal structure description

For the two complexes **C1** and **C2**, which crystallise in needles, X-ray structure data were obtained at 120 K.

Complex **C1** crystallises in an orthorhombic crystal system in the *Pbcn* space group with two formula units per unit cell. Detailed crystallographic information can be found in Table S1. The complex adopts a square planar geometry (Fig. 2). The Cu–N distance is 1.938 (2) Å, the Cu–O distance 1.9013 (19) Å. The molecules are stacked in layers along the *c*-axis, forming an ABAB sequence. The distance between each layer is 3.425(1) Å (Fig. S9).

Complex **C2** crystallises in monoclinic crystal system in the C_2/c space group, additional crystallographic information can be found in Table S1. The complex also adopts a square planar geometry. The Ni–N distance is 1.8427(18) Å and the Ni–O bond length is 1.8488(15) Å. Similar to complex **C1**, the individual molecules within the crystal lattice are arranged in layers along the *c*-axis, forming an ABAB sequence. The distance between each layer is determined to be 3.396 Å (Fig. S10).

Electrocatalytic hydrogen production

Cyclic voltammetry measurements were carried out on complexes **C1** and **C2**. The CV experiments were conducted using a three-electrode system with a glassy carbon working electrode, an Ag/$AgNO_3$ reference electrode, and a platinum counter electrode. The electrolyte solution consisted of tetrabutylammonium hexafluorophosphate as electrolyte (0.1 M) and complex **C1** or **C2** (0.5 mM) in dried DMF. It was purged with

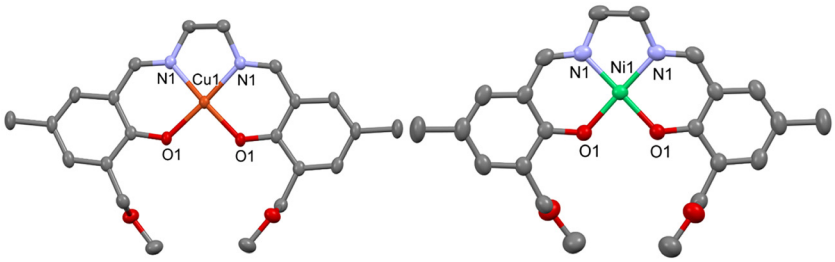

C1 C2

Fig. 2 X-ray crystal structures of complex $[Cu^{II}(H_2L^{Me})]\cdot 1.5H_2O$ (**C1**) and $[Ni^{II}(H_2L^{Me})]\cdot 3H_2O$ (**C2**).

argon for 20 minutes prior to the measurement. Unless otherwise specified, all potentials mentioned are referenced to the ferrocenium redox couple ($Fc^{0/+}$). For $[Cu^{II}L^{Me}]\cdot 1.5H_2O$ (**C1**) distinct waves in the CV data are observed at $E_{1/2}$ = −1.21 V and $E_{1/2}$ = −1.59 V, and are assigned to the $Cu^{II}L/Cu^{I}L$ and LH_4/LH_4^- redox process, respectively.[28] On the other hand, $[Ni^{II}L^{Me}]\cdot 3H_2O$ (**C2**) shows a single peak at $E_{1/2}$ = −2.09 V, corresponding to the $Ni^{II}L/Ni^{I}L$ redox process, and another at $E_{1/2}$ = +0.39 V, associated with the $Ni^{II}L/Ni^{III}L$ redox process (Fig. 3).[29] These assignments are in agreement with redox waves observed for nickel complexes with salen type ligands reported in the literature.[28] The assignment for copper complex processes were made based on the CV of the ligand (Fig. S22).

The difference in anodic peak potentials of more than 100 mV indicates quasi-reversible redox processes. Scan rate studies performed for both the complexes (Fig. S20 and S21) revealed, as predicted for quasi-reversible processes, a shift in peak potentials with increasing scan rates, accompanied by a corresponding increase in current.

The electrocatalytic proton reduction activity of both complexes **C1** and **C2** was evaluated in DMF under Argon atmosphere with acetic acid as a proton source. The use of acetic acid offers several advantages: (a) it is a weak acid (pK_a = 13.5 in DMF) and therefore allows prolonged catalytic activity, and (b) its polar nature reduces homoconjugation in DMF.[30]

The addition of acetic acid initiated the emergence of a peak shaped non-reversible catalytic wave in the CV, as seen in Fig. 4. In the absence of the catalysts **C1** and **C2** the electrocatalytic reduction of acetic acid is kinetically very demanding, with no significant increase in the electrolytic current observed during the cathodic sweeping until −2.3 V (Fig. S23).

In the case of **C1**, the addition of acetic acid (Fig. 4 left) results in the appearance of two pre-waves at −1.27 V and −1.68 V, and an onset potential for HER is observed at −2.04 V, indicating the catalytic activity of the material. The pre-waves, corresponding to the CV in the absence of substrate, suggest that after the initial reduction process, further reduction of the resulting species under more negative potentials is required for catalytic hydrogen production to occur, indicating a heterolytic HER mechanism.[31] Similarly, for complex **C2**, a pre-wave ahead of the actual catalytic wave can be observed in the cyclic voltammograms (Fig. 4; right).[29–31]

After adding 60 mM acid, the catalytic current exceeds 100 μA for both **C1** and **C2**. Furthermore, a crossing of the catalytic waves can be observed for **C2**. This may indicate time-dependent activation or structural changes of the catalyst.[32] Based on the catalytic current maximum, preliminary findings show that complex **C1** is slightly more active than complex **C2**. The $E_{cat/2}$, known from the literature as the potential at which half the maximum catalytic current is achieved, is calculated to be −2.2 V for complex **C1** and −2.4 V for complex **C2**.

To evaluate the electrocatalytic activity, a foot-of-the-wave analysis was employed, focusing on the region following the onset potential of the HER catalytic wave.

The FOWA plots for **C1** and **C2**, depicted in Fig. 5, were subsequently fitted in their linear segments. The fitting yielded the necessary slope, allowing the calculation of TOF_{max} as 452 029 s^{-1} for **C1** and 986 s^{-1} for **C2**, which is therefore over 400 times less than the copper complex **C1**. It should be emphasised, however, that the TOF_{max} value derived for **C1** must be interpreted with caution. After electrolysis, analysis revealed the formation of a heterogeneous Cu^0 deposit on the electrode surface following bulk electrolysis. As a result, the high TOF_{max} estimated for **C1** is unlikely to reflect the intrinsic

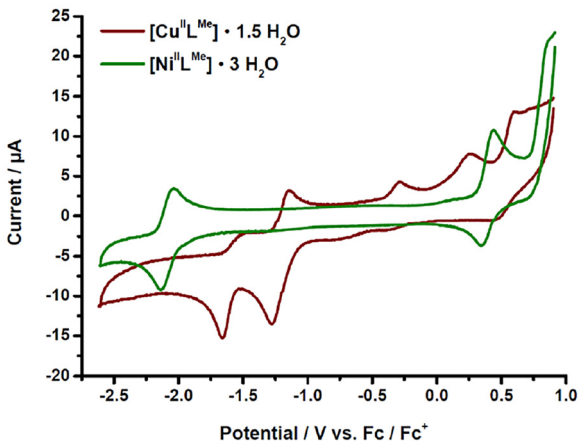

Fig. 3 Cyclic voltametric study of complex $[Cu^{II}L^{Me}]\cdot 1.5H_2O$ **C1** (red) and $[Ni^{II}L^{Me}]\cdot 3H_2O$ **C2** (green).

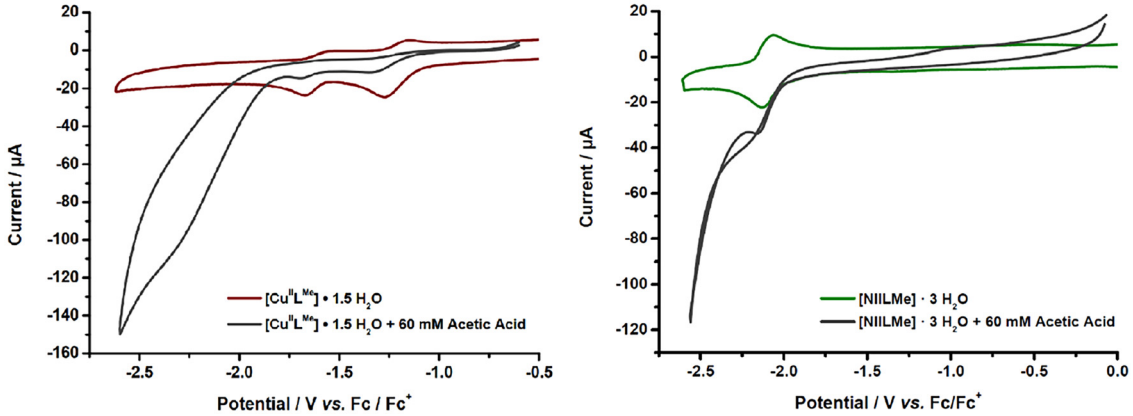

Fig. 4 Cyclic voltammograms of $[Cu^{II}L^{Me}]\cdot 1.5H_2O$ (**C1**) (left) and $[Ni^{II}L^{Me}]\cdot 3H_2O$ (**C2**) (right) in DMF (0.05 mM) with acetic acid (60 mM) at a scan rate of 0.05 V s^{-1}.

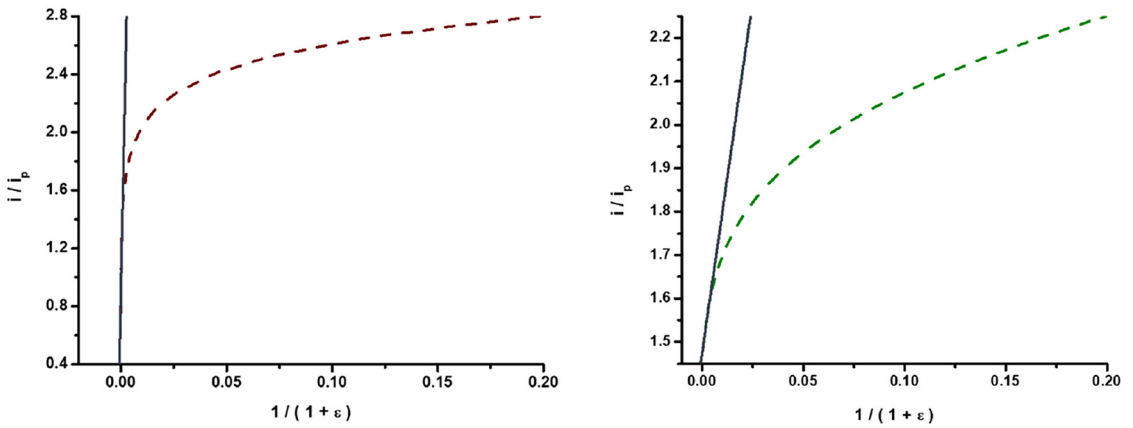

Fig. 5 FOWA plot of $[Cu^{II}L^{Me}]\cdot 1.5H_2O$ (**C1**) (left) and $[Ni^{II}L^{Me}]\cdot 3H_2O$ (**C2**) (right): i/i_p plotted according to FOWA starting from onset potential of the catalytic wave.

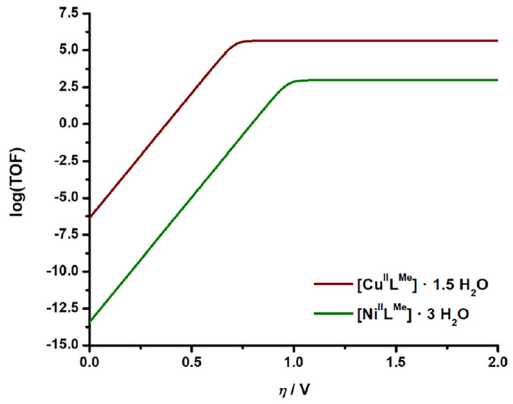

Fig. 6 Tafel plot: calculated log(TOF) plotted against applied overpotential η for $[Cu^{II}L^{Me}]\cdot 1.5H_2O$ (**C1**) (red) and $[Ni^{II}L^{Me}]\cdot 3H_2O$ (**C2**) (green).

activity of a purely molecular catalyst and may be significantly inflated by contributions from heterogeneous copper species, which will be discussed in detail in the following sections.

For a more visual comparison of the activity of both catalysts, we employed Tafel analysis by plotting the logarithm of the turnover frequency, log(TOF), against the overpotential η, as shown in Fig. 6. The overpotential required for the catalytic reaction to occur is calculated by subtracting the reduction potential of acetic acid under given conditions from the applied potential E. Based on the Nernst equation Dempsey *et al.* have defined a relationship to calculate the thermodynamic potential for proton reduction to dihydrogen in non-aqueous solvents, for given standard potential $E^{\circ}_{H^+/H_2}$ and acid strength of the proton source pK_a in the solvent of choice.[32]

$$E_{HA/H_2} = E^{\circ}_{H^+/H_2} - \frac{2.303 \cdot R \cdot T}{F} \cdot pK_a$$

With the given values for acetic acid in DMF the reduction potential was calculated to be 1.46 V *vs.* Fc/Fc^+.[12,28] As expected from the TOF_{max} values, we observe a significant difference between the copper complex **C1** ($\log(TOF_{max})$ = 5.7) and the nickel complex **C2** ($\log(TOF_{max})$ = 3.0). Furthermore, the overpotential at which the catalytic reaction occurs highlights the

superior catalytic performance of **C1** in the hydrogen evolution reaction, with η = 0.89 V.

Overpotentials are commonly used to compare the catalytic activity with analogues from literature. Electrocatalytic hydrogen evolution reactions (HER) have been extensively studied, with copper and especially nickel-based catalysts emerging as prominent candidates due to their earth abundance and cost-effectiveness. However, their catalytic performance varies significantly depending on their composition and structure. Further, when comparing overpotentials, the following factors such as the pH, solvent and the reference electrode used to measure and report the potential, must be considered. Considering the above parameters, **C1** and **C2** seem to compare well with the literature values for Cu and Ni analogues reported by Zhao-Qing Liu and co-workers on an analogue catalytic salen system. Their results showed overpotentials of 0.61 V and 0.51 V *vs.* $Fc^{+/0}$ in MeCN for salen derivative nickel and copper complexes, respectively.[27] Further, Shu-Zhong Zhan and co-workers reported a salen derivated Cu(II) catalyst with an overpotential of 0.82 V *vs.* SHE in H_2O.[26]

While salen-type ligands have been widely studied, non-salen ligand systems have also shown promising activity. For copper-based HER electrocatalysts, Brooker and co-workers reported a square planar $[Cu^{II}L^{Et}]$ BF_4 complex exhibiting an overpotential of 230 mV in MeCN with acetic acid, with stable performance attributed to a homogeneous mechanism.[12] The imine-type nickel complex by Le *et al.* requires higher overpotentials (590 mV in DMF with acetic acid), but shows mechanistic features such as ligand-centered electron transfer that can be exploited for catalyst design.[33]

In comparison, our copper complex **C1** exhibits an overpotential of 0.71 V and the nickel complex **C2** an overpotential of 0.89 V under the tested conditions, which are within the range of reported values for both salen and non-salen copper and nickel complexes. These results suggest that the new ligand framework employed here provides competitive activity, and further optimization could yield even lower overpotentials.

Control potential electrolysis (CPE) and quantification

To further investigate the catalytic activity of **C1** and **C2**, controlled potential electrolysis was carried out using a glassy carbon electrode (d = 0.3 cm, A = 0.07 cm^2). As shown in Fig. 7, the plain acid in the absence of catalyst shows very low activity, whereas both complexes **C1** and **C2** show good catalytic activity with a charge accumulation of 1.42 C for **C1** at −1.95 V and 1.12 C for **C2** at −2.05 V over two hours. Control experiments were conducted with a freshly prepared electrolyte solution after electrolysis (Fig. 7) to check the homogeneous nature of the catalytic activity in **C1** and **C2**. In the case of **C1**, the rinse test carried out at −1.95 V showed some activity, with a charge accumulation of 0.70 C over two hours. The rinse test for the nickel complex **C2** revealed a charge accumulation of 0.75 C at −2.05 V over the same two-hour period. To further explore the nature of the electrode deposition and its influence on catalytic performance, additional measurements were conducted for both complexes at several different potentials (S24–S29).

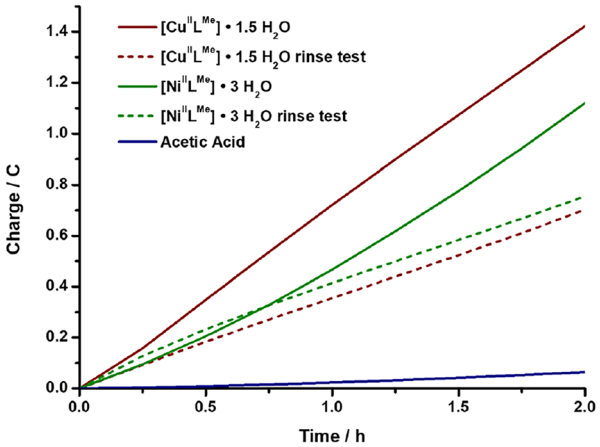

Fig. 7 Charge transferred during control potential electrolysis at −1.95 V for **C1** (red solid line) and −2.05 V for **C2** (green solid line). After the electrolysis of **C1** and **C2** the glassy carbon electrode was gently rinsed with DMF, and electrolysis was repeated in a freshly prepared electrolyte solution with 60 mM acetic acid but with no addition of catalyst. The dotted lines are the rinse test (red **C1** and green **C2**).

To rule out the possibility of nanoparticle formation during the electrolysis the reaction solutions of both complexes were analysed by Dynamic Light Scattering (DLS) technique after two hours of CPE and no nanoparticles were detected (Fig. S46). The morphology and composition of the deposited material were further analysed by SEM and EDX analysis, which will be discussed below.

To quantify the amount of hydrogen produced during electrolysis, the evolved gas was collected in a sealed cell and analysed using gas chromatography. The total volume of hydrogen generated over the electrolysis period was recorded, and the corresponding charge passed was noted from the electrochemical data.

For complex **C1**, the total amount of hydrogen evolved after two hours was 4.21 μmol, corresponding to a faradaic efficiency of 75%, calculated based on the total charge passed during electrolysis (Q = 1.07 C). The average hydrogen production rate was therefore 2.11 μmol h^{-1}. For the rinse test, after the initial electrolysis, the electrode was rinsed, then immersed in a fresh electrolyte solution without the catalyst, and electrolysis was performed again under identical conditions. The hydrogen evolution during this rinse test was 1.22 μmol, corresponding to a faradaic efficiency of 83%, indicating that some catalytic species, likely deposited on the electrode surface during the initial electrolysis, remain active in the absence of the homogeneous catalyst in solution. These results imply that while the homogeneous catalyst plays a role, the electrode-bound deposit also contributes to the overall activity observed during the initial electrolysis.

Similarly, for complex **C2**, the total hydrogen evolved was 2.73 μmol, with a faradaic efficiency of 87%, and an average production rate of 1.37 μmol h^{-1}. Compared to complex **C1**, which achieved a greater total hydrogen evolution, **C2** operates more efficiently in terms of electron utilization, which directly

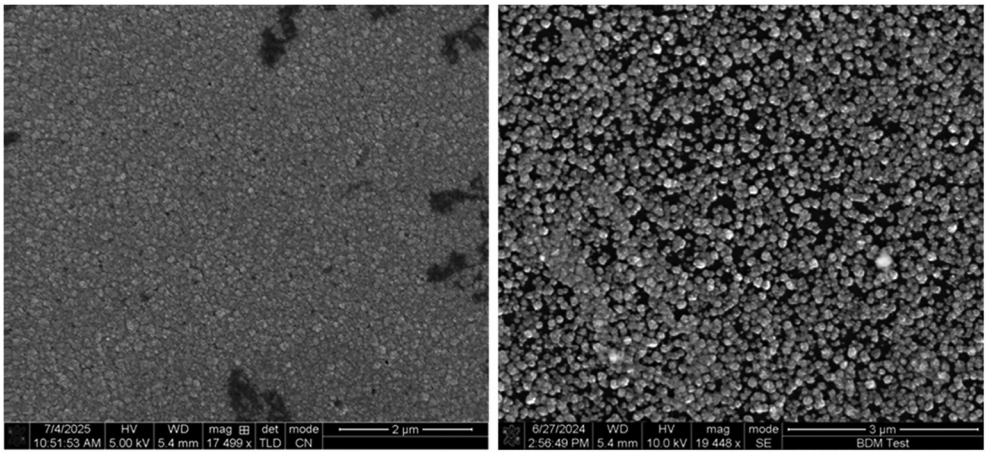

Fig. 8 SEM images of deposition on glassy carbon plate after 3 h bulk electrolysis for copper complex $[Cu^{II}L^{Me}]\cdot 1.5H_2O$ (**C1**) (left) and $[Ni^{II}L^{Me}]\cdot 3H_2O$ (**C2**) (right).

correlates with the relative stability of the complexes. **C1** appears to form electrode-bound deposits that retain catalytical activity, while **C2** remains more homogeneous and potentially more stable under the same conditions.

Surface analysis of the working electrode after electrolysis

To better understand the nature of the catalytic species involved in HER, the working electrode surfaces were analysed following controlled potential electrolysis (CPE) of both complexes **C1** and **C2**. SEM imaging (S32–S33) revealed the formation of aggregated, spherical structures on the electrode surface in both cases (Fig. 8).

EDX analysis was performed on both complexes **C1** and **C2** at three different representative regions on the working electrode: (i) a region of a bare, uncoated glassy carbon electrode, (ii) the edge of the deposited area, and (iii) in the centre of the deposited region. As anticipated, the bare region of the electrode showed almost no elements apart from carbon from the glassy carbon electrode (Fig. S42–S45 and Tables S12–S13). At the edge of the deposition surface carbon still dominated, with some amounts of Cu (19.5%) for **C1** and barely any Ni (0.1%) for **C2**, along with traces of nitrogen and oxygen (Fig. S38–S41 and Tables S10–S11). The central regions of the deposit for **C1** contained significantly higher copper content (54.9%), while the corresponding region for **C2** revealed only 0.4% nickel (Fig. S34–S37 and Tables S8–S9).

This clearly indicates that the complex has decomposed upon electrodeposition during catalysis, most likely to elemental Cu^0 with some traces of Cu_2O species, both of which are known to be very active for hydrogen production from the literature.[34,35] In contrast, the low nickel content detected for **C2** indicates limited deposition and therefore higher homogeneous stability compared to **C1**. However, the rinse tests reveal these nickel-derived deposits to be catalytically active, accumulating charges comparable to the ones accumulated by the deposition of **C1**, contributing to the overall HER process.

Despite the superior catalytic performance of the copper complex, as indicated by its lower overpotential and significantly higher TOF_{max}, the deposition observed in SEM/EDX and the high activity collected on the rinsed electrode suggest a transformation into heterogeneous species, highlighting its lower stability under homogeneous catalytic conditions. On the other hand, the nickel complex, though less active overall, demonstrated greater stability under catalytic conditions, as shown by the minimal deposition. Dynamic light scattering (DLS) measurements performed on the post-electrolysis solutions confirmed the absence of nanoparticles, affirming that all catalytic activity arose either from the molecular complex in solution or from species deposited on the electrode surface.

Conclusion

In this paper we report the multistep synthesis of 2,6-bis (hydroxymethyl)-4-methylphenol ligand $H_4\mathbf{L}$ and two corresponding complexes $[Cu^{II}(H_2\mathbf{L^{Me}})]\cdot 1.5H_2O$ (**C1**) and $[Ni^{II}(H_2\mathbf{L^{Me}})]\cdot 3H_2O$ (**C2**). The complexes were synthesised and characterised by various techniques. Structural analysis revealed square planar geometries for the central metal ions and layered molecular arrangements for both complexes. Electrochemical investigations demonstrated that both **C1** and **C2** exhibit catalytic activity for hydrogen evolution in DMF with acetic acid, with **C1** showing slightly higher activity and lower overpotential compared to **C2**. Controlled potential electrolysis confirmed that the catalytic processes involve both homogeneous and heterogeneous contributions, as evidenced by rinse tests and surface deposit analyses. Surface characterization *via* SEM and EDX indicated that the complexes undergo transformation during electrolysis, forming metallic copper and likely nickel deposits on the electrode surface, which contribute to catalytic activity. Importantly, DLS measurements ruled out nanoparticle formation in solutions. To preserve the homogeneous catalytic activity and increase the stability,

ongoing work focuses on immobilising the complexes on the working electrode prior to testing. Studies are also being undertaken to recover the heterogeneous deposit for reuse in the preparation of new catalytic material.

Experimental

All chemicals were purchased from Alfa Aesar, Deutero, Fisher Chemicals, TCI, Sigma-Aldrich, and Acros Organics and used without further purification. Solvents were dried according to the literature known procedures and used freshly distilled.[36] Dry DMF was purchased from Sigma Aldrich. NMR spectra were recorded at room temperature with a Bruker Avance DSX 400 and analysed with the program MestReNova.[36] All elemental analysis (Elementar vario EL Cube: C, H, and N) were measured at the microanalytical laboratories of the Johannes Gutenberg University Mainz. X-ray diffraction data were collected with STOE STADIVARI at the Johannes Gutenberg University Mainz. The structures were solved with ShelXT[37] and refined with ShelXL[37,38] implemented in the program Olex2.[39] The X-ray cif file data are deposited on the Cambridge CCDC database with identification numbers 2409307 and 2409308. All the cyclic voltammetry and electrolysis measurements were carried out with a PARSTAT MC Multichannel Potentiostat. The quantification experiments were carried out with the Shimadzu GC2030 gas chromatograph equipped with a barrier ionization discharge (BID) detector. High-purity helium (He, 99.999%) was used as carrier gas.

Ligand synthesis

Synthesis of 2-hydroxy-3-(hydroxymethyl)-5-methylbenzaldehyde. The synthesis of 6-(hydroxymethyl)-5-methylbenzaldehyd was performed as described by Ru-Gang Xie Wang *et al.*[40] 2,6-bis(hydroxymethyl)-4-methylphenol (5.00 g, 30 mmol, 1.00 eq.) was added to 500 ml of chloroform. Manganese dioxide (16.00 g, 184 mmol, 6.13 eq.) was added to the cloudy, slightly pink reaction solution in small portions over nine hours. The black reaction mixture was stirred overnight at room temperature and then filtered over Celite, resulting in a brown to yellow solution. The solvent was removed under reduced pressure and the product was purified and separated from the dialdehyde by column chromatography (R_f = 0.15 (*n*-hexane/EtOAc = 72/28) TLC: PF-30SIHPF0040-coloumn; 26.0 mL min^{-1}; 1 bar; injection valve mode, Dryload, PF-DLE-F0004.) and obtained as a white solid in moderate yields (3.04 g, 18.3 mmol, 61%). ^{1}H-NMR ($CDCl_3$, 400 MHz) δ/ppm: 2.37 (s, 3H, H 4); 4.76 (s, 2H, H 2); 7.32 (d, 2.2 Hz, 1H, H 3); 7.43 (d, 2.3 Hz, 1H, H 5); 9.89 (s, 1H, H 6); 11.21 (s, 1H, H 1). IR $\tilde{\nu}$ (cm^{-1}): 3170 (w), 1626 (s), 1567 (m), 1457 (m), 1388 (w), 1333 (w), 1293 (m), 1271 (m), 1243 (m), 1224 (w), 1182 (w), 1082 (ss), 1002 (m), 963 (m), 918 (m), 868 (m), 813 (m), 761 (m), 621 (ss), 535 (m), 440 (m), 406 (s).

Synthesis of H_4L ligand. The Ligand was synthesised as described by Mahammad Ali *et al.*[41] 2-hydroxy-3-(hydroxymethyl)-5-methylbenzaldehyde (2.45 g, 14.70 mmol, 1 eq.) was dissolved in 45 mL of methanol and ethylenediamine (0.44 g, 7.35 mmol, 0.50 eq. 0.49 mL) dissolved in 5 mL of methanol was added over a few minutes. The reaction mixture was stirred for two hours under reflux conditions and stored overnight in the refrigerator. The yellow precipitate was isolated in high yields through vacuum filtration and finally dried in the air (2.03 g, 6.45 mmol, 88%). ^{1}H-NMR ($CDCl_3$, 400 MHz) δ/ppm: 2.29 (s, 6H, H 1,1 0); 3.96 (s, 4H, H 13,130); 4.73 (s, 4H, H 10,100/13); 7.01 (s, 2H, H 7,7 0); 7.14 (s, 2H, H 3,3 0); 8.35 (s, 2H, H 8,8 0); 9.89 (s, 2H, H 9,9 0); 11.21 (s, 2H, H 11,110). 13C {1H}-NMR ($CDCl_3$, 101 MHz) δ/ppm: 20.3 (C 1,1 0); 59.5 (C 10,100); 61.9 (C 13,130); 118.0 (C 6,6 0); 127.6 (C 4,4 0); 128.3 (C 7,7 0); 130.9 (C 2 0, 9 0); 132.7 (C 3,3 0); 157.3 (C 5,5 0); 166.5 (C 8,8 0). IR $\tilde{\nu}$ (cm^{-1}): 3303 (w); 2912 (w); 2860 (w); 1628 (w); 1600 (w); 1460 (w); 1444 (w); 1373 (w); 1333 (w); 1249 (w); 1211 (w); 1163 (w); 1096 (w); 1074 (w); 1041 (w); 1005 (w); 955 (w); 876 (w); 864 (w); 847 (w); 792 (w); 755 (w); 746 (w); 719 (w); 649 (w); 606 (w); 581 (w); 568 (w); 467 (w). Elemental Analysis calculated for $H_4L{\cdot}3.5H_2O$: C, 57.27; H, 7.45; N, 6.88; found: C, 57.46; H, 6.69; N, 6.42.

Complex synthesis

Synthesis of $[Cu^{II}(L^{Me})]{\cdot}1.5H_2O$ (C1). H_4L (0.18 g, 0.50 mmol, 1.00 eq.) was dissolved in methanol (15 mL) and $Cu(ClO_4)_2{\cdot}6H_2O$ (0.19 g, 0.50 mmol, 1.00 eq.) was added while stirring, whereupon the previously yellow solution turned dark brown. The reaction mixture was stirred at 80 °C for two hours and then filtered while hot. After one week of slow evaporation violet, needle-like crystals were formed. IR $\tilde{\nu}$ (cm^{-1}): 2968 (m), 2857 (m), 2797 (m), 1632 (ss), 1544 (s), 1440 (s), 1382 (s), 1335 (m), 1318 (s), 1268 (m), 1240 (m), 1226 (m), 1188 (m), 1171 (m), 1091 (ss), 1043 (s), 1006 (m), 962 (m), 944 (s), 895 (s), 856 (s), 804 (s), 781 (s), 657 (m), 622 (m), 601 (m), 571 (m), 563 (m), 541 (m), 504 (s), 485 (m), 455 (m), 433 (m). Elemental analysis calculated for $C_{22}H_{26}CuN_2O_4{\cdot}1.5H_2O$: C, 56.00%; H, 6.29%; N, 6.19. Found: C, 55.86; H, 6.18; N, 5.92%.

Synthesis of $[Ni^{II}(L^{Me})]{\cdot}3H_2O$ (C2). H_4L (0.178 g, 0.5 mmol) was dissolved in methanol (15 mL) and $Ni(ClO_4)_2{\cdot}6H_2O$ (0.183 g, 0.5 mmol) was added while stirring, whereupon the previously yellow solution turned orange. The reaction mixture was stirred at 80 °C for two hours and then filtered while hot. After a week of slow evaporation orange, needle-like crystals were obtained. IR $\tilde{\nu}$ (cm^{-1}): 2855 (m), 1620 (m), 1545 (s), 1443 (m), 1382 (m), 1307 (m), 1269 (m), 1226 (m), 1189 (m), 1169 (m), 1089 (s), 1019 (m), 941 (s), 890 (m), 855 (s), 811 (m), 777 (m), 725 (m), 631 (m), 594 (m), 564 (m), 524 (m), 406 (ss). Elemental analysis calculated $C_{22}H_{26}N_2NiO_4{\cdot}3H_2O$: C, 53.36%; H, 6.51%; N, 5.66%. Found, C; 53.16%, H, 6.37; N, 5.91.

Conflicts of interest

The authors have no conflict of interest to declare.

Data availability

All the processed data supporting the findings of this study are available within the article and supplementary information (SI). Supplementary information is available. See DOI: https://doi.org/10.1039/d6dt00175k.

All the raw data files supporting this publication are available from the Figshare at https://doi.org/10.6084/m9.figshare.28046039 and https://doi.org/10.5281/zenodo.17279986.

CCDC 2409307 and 2409308 contain the supplementary crystallographic data for this paper.[42a,b]

Acknowledgements

All the authors sincerely thank JGU Mainz for the funding and support. SS and M. A. B. specially thank JGU Mainz for the startup research grant Stufe I for the catalysis project. CS thanks the Deutsche Forschungsgemeinschaft (DFG, German Research Foundation) – 364549901 for financial support. We also thank Mr Sven Schäfer and Prof. Dr Sebastian Seiffert for the DLS measurements. SS and M. A. B. would also like to thank Dr Rongji Liu for introducing us to the electrochemistry gear used for the measurements and for the scientific discussions. SS and M. A. B. thank Ms Isabell Erdmann and Dr Ute Kolb for the SEM-EDX measurements.

References

1 L. Xu, K. Feng, N. Lin, A. T. D. Perera, H. Vincent Poor, L. Xie, C. Ji, X. A. Sun, Q. Guo and M. O'Malley, *Nat. Rev. Electr. Eng.*, 2024, **1**, 53–66.
2 A. Risco-Bravo, C. Varela, J. Bartels and E. Zondervan, *Renewable Sustainable Energy Rev.*, 2024, **189**, 1364–0321.
3 L. Fan, Z. Tu and S. H. Chan, *Energy Rep.*, 2021, **7**, 8421–8446.
4 A. Odenweller, F. Ueckerdt, G. F. Nemet, M. Jensterle and G. Luderer, *Nat. Energy*, 2022, **7**, 854–865.
5 D. Liu, X. Li, S. Chen, H. Yan, C. Wang, C. Wu, Y. A. Haleem, S. Duan, J. Lu, B. Ge, P. M. Ajayan, Y. Luo, J. Jiang and L. Song, *Nat. Energy*, 2019, **4**, 512–518.
6 N. Cheng, S. Stambula, D. Wang, M. N. Banis, J. Liu, A. Riese, B. Xiao, R. Li, T. K. Sham, L. M. Liu, G. A. Botton and X. Sun, *Nat. Commun.*, 2016, **7**, 1–9.
7 S. Losse, J. G. Vos and S. Rau, *Coord. Chem. Rev.*, 2010, **254**, 2492–2504.
8 K. E. Dalle, J. Warnan, J. J. Leung, B. Reuillard, I. S. Karmel and E. Reisner, *Chem. Rev.*, 2019, **119**, 2752–2875.
9 R. W. Hogue, O. Schott, G. S. Hanan and S. Brooker, *Chem. – Eur. J.*, 2018, **24**, 9820–9832.
10 N. Queyriaux, R. T. Jane, J. Massin, V. Artero and M. Chavarot-Kerlidou, *Coord. Chem. Rev.*, 2015, **304–305**, 3–19.
11 D. Basu, S. Mazumder, J. Niklas, H. Baydoun, D. Wanniarachchi, X. Shi, R. J. Staples, O. Poluektov, H. B. Schlegel and C. N. Verani, *Chem. Sci.*, 2016, **7**, 3264–3278.
12 A. M. Abudayyeh, O. Schott, H. L. C. Feltham, G. S. Hanan and S. Brooker, *Inorg. Chem. Front.*, 2021, **8**, 1029.
13 E. S. Andreiadis, M. Chavarot-Kerlidou, M. Fontecave and V. Artero, *Photochem. Photobiol.*, 2011, **87**, 946–964.
14 C. G. Morales-Guio, S. D. Tilley, H. Vrubel, M. Grätzel and X. Hu, *Nat. Commun.*, 2014, **5**, 3059.
15 P. Zhang, M. Wang, Y. Yang, T. Yao and L. Sun, *Angew. Chem., Int. Ed.*, 2014, **53**, 13803–13807.
16 S. Fukuzumi, Y. Yamada, T. Suenobu, K. Ohkubo and H. Kotani, *Energy Environ. Sci.*, 2011, **4**, 2754.
17 V. Artero and M. Fontecave, *Chem. Soc. Rev.*, 2013, **42**, 2338–2356.
18 B. H. Solis and S. Hammes-Schiffer, *J. Am. Chem. Soc.*, 2011, **133**, 19036–19039.
19 A. Panagiotopoulos, K. Ladomenou, D. Sun, V. Artero and A. G. Coutsolelos, *Dalton Trans.*, 2016, **45**, 6732.
20 V. Artero and J.-M. Saveant, *Energy Environ. Sci.*, 2014, **7**, 3808–3814.
21 M. Kügler, J. Scholz, A. Kronz and I. Siewert, *Dalton Trans.*, 2016, **45**, 6974–6982.
22 A. Friedman, K. Yang, H. Ge and S. Mukerjee, *ACS Catal.*, 2025, **15**, 7040–7052.
23 T. B. Rauchfuss, *Acc. Chem. Res.*, 2015, **48**, 2107–2116.
24 R. M. Clarke, K. Herasymchuk and T. Storr, *Coord. Chem. Rev.*, 2017, **352**, 67–82.
25 M. Karmakar and S. Chattopadhyay, *J. Mol. Struct.*, 2019, **1186**, 155–186.
26 J. P. Cao, T. Fang, L. Z. Fu, L. L. Zhou and S. Z. Zhan, *Int. J. Hydrogen Energy*, 2014, **39**, 13972–13978.
27 X. S. Hong, D. Huo, W. J. Jiang, W. J. Long, J. D. Leng, L. Tong and Z. Q. Liu, *ChemElectroChem*, 2020, **7**, 4956–4962.
28 E. Deunf, E. Zaborova, S. Guieu, Y. Blériot, J. N. Verpeaux, O. Buriez, M. Sollogoub and C. Amatore, *Eur. J. Inorg. Chem.*, 2010, 4720–4727.
29 Q. Lin, G. Dawson and T. Diao, *Synlett*, 2021, 1606–1620.
30 F. Maran, D. Celadon, M. G. Severin and E. Vianello, *J. Am. Chem. Soc.*, 1991, **113**, 9320–9329.
31 X. Guo, N. Wang, X. Li, Z. Zhang, J. Zhao, W. Ren, S. Ding, G. Xu, J. Li, U. Apfel, W. Zhang and R. Cao, *Angew. Chem., Int. Ed.*, 2020, **59**, 8941–8946.
32 K. J. Lee, B. D. McCarthy and J. L. Dempsey, *Chem. Soc. Rev.*, 2019, **48**, 2927–2945.
33 L. H. Le, N. H. Pham, P. D. Tran and T. H. To, *RSC Adv.*, 2025, **15**, 2430–2436.
34 M. Kügler, J. Scholz, A. Kronz and I. Siewert, *Dalton Trans.*, 2016, **45**, 6974–6982.
35 A. M. Abudayyeh, M. S. Bennington, J. Hamonnet, A. T. Marshall and S. Brooker, *Dalton Trans.*, 2024, **53**, 6207–6214.
36 J. C. Cobas and F. J. Sardina, *Concepts Magn. Reson., Part A*, 2003, **19**, 80–96.
37 G. M. Sheldrick, *Acta Crystallogr., Sect. C: Struct. Chem.*, 2015, **71**, 3–8.

38 G. M. Sheldrick and T. R. Schneider, *Methods Enzymol.*, 1997, **277**, 319–343.
39 O. V. Dolomanov, L. J. Bourhis, R. J. Gildea, J. A. K. Howard and H. Puschmann, *J. Appl. Crystallogr.*, 2009, **42**, 339–341.
40 R.-G. Xie, Z.-J. Zhang, J.-M. Yan and D.-Q. Yuan, *Synth. Commun.*, 1994, **24**, 53–58.
41 S. Biswas, A. Dutta, M. Dolai, M. Debnath, A. D. Jana and M. Ali, *RSC Adv.*, 2014, **4**, 34248–34256.
42 (*a*) CCDC 2409307: Experimental Crystal Structure Determination, 2026, DOI: 10.5517/ccdc.csd.cc2lw2l5; (*b*) CCDC 2409308: Experimental Crystal Structure Determination, 2026, DOI: 10.5517/ccdc.csd.cc2lw2m6.